



IC 5146 Dark Streamer: The First Reliable Candidate of Edge Collapse, Hub-filament Systems, and Intertwined Sub-filaments

L. K. Dewangan¹ , N. K. Bhadari^{1,2} , A. Men'shchikov³ , E. J. Chung⁴ , R. Devaraj⁵ , C. W. Lee^{6,7} ,
A. K. Maity^{1,2} , and T. Baug⁸

¹ Astronomy & Astrophysics Division, Physical Research Laboratory, Navrangpura, Ahmedabad 380009, India; lokeshd@prl.res.in

² Indian Institute of Technology Gandhinagar Palaj, Gandhinagar 382355, India

³ Université Paris-Saclay, Université Paris Cité, CEA, CNRS, AIM, F-91191, Gif-sur-Yvette, France

⁴ Department of Astronomy and Space Science, Chungnam National University, Daejeon, Republic of Korea

⁵ Dublin Institute for Advanced Studies, 31 Fitzwilliam Place, Dublin D02XF86, Ireland

⁶ Korea Astronomy and Space Science Institute, 776 Daedeokdae-ro, Yuseong-gu, Daejeon 34055, Republic of Korea

⁷ University of Science and Technology, Korea (UST), 217 Gajeong-ro, Yuseong-gu, Daejeon 34113, Republic of Korea

⁸ Satyendra Nath Bose National Centre for Basic Sciences, Block-JD, Sector-III, Salt Lake, Kolkata-700 106, India

Received 2022 December 8; revised 2023 February 14; accepted 2023 February 14; published 2023 March 23

Abstract

The paper presents an analysis of multiwavelength data of a nearby star-forming site, the IC 5146 dark streamer ($d \sim 600$ pc), which has been treated as a single and long filament, *fl*. Two hub-filament systems (HFSs) are known to exist toward the eastern and the western ends of *fl*. Earlier published results favor simultaneous evidence of HFSs and end-dominated collapse (EDC) in *fl*. A Herschel column density map (resolution $\sim 13''$) reveals two intertwined sub-filaments (i.e., *fl-A* and *fl-B*) toward *fl*, displaying a nearly double helix-like structure. This picture is also supported by the $C^{18}O(3-2)$ emission. The *fray and fragment* scenario may explain the origin of intertwined sub-filaments. In the direction of *fl*, two cloud components around 2 and 4 km s⁻¹ are depicted using $^{13}CO(1-0)$ and $C^{18}O(1-0)$ emission and are connected in velocity space. The HFSs are spatially found at the overlapping areas of these cloud components and can be explained by the cloud–cloud collision scenario. Nonthermal gas motion in *fl* with a larger Mach number is found. The magnetic field position angle measured from the filament's long axis shows a linear trend along the filament. This signature is confirmed in the other nearby EDC filaments, presenting a more quantitative confirmation of the EDC scenario. Based on our observational outcomes, we witness multiple processes operational in the IC 5146 streamer. Overall, the streamer can be recognized as the first reliable candidate for edge collapse, HFSs, and intertwined sub-filaments.

Unified Astronomy Thesaurus concepts: Star forming regions (1565); H II regions (694); Molecular clouds (1072); Interstellar emissions (840); Young stellar objects (1834)

1. Introduction

Several studies of star-forming regions (SFRs) have revealed that dust and molecular filaments are actively involved in star formation processes. In SFRs, a system of filaments converging to a central hub, which is referred to as a hub-filament system (HFS; Myers 2009), is a commonly observed feature, where young stellar objects (YSOs) and massive OB stars ($M \gtrsim 8 M_{\odot}$) are born. Furthermore, researchers have also identified isolated filaments undergoing end-dominated collapse (EDC) or edge collapse (Bastien 1983; Pon et al. 2012; Clarke & Whitworth 2015), and observational evidence of such EDC filaments is gradually increasing in the literature (e.g., NGC 6334 (Zernickel et al. 2013), Sh 2-242 (or S242; Dewangan et al. 2019; Yuan et al. 2020), IC 5146 (Wang et al. 2019; Chung et al. 2022), Mon R1 (or Mon R1; Bhadari et al. 2020), G341.244-00.265 (Yu et al. 2019), and G45.3+0.1 (Bhadari et al. 2022)). Using a multiwavelength approach, a few SFRs have been identified and reported, where the edge collapse and the HFSs have been simultaneously investigated (e.g., G45.3+0.1 Bhadari et al. 2022; IC 5146 dark streamer Wang et al. 2019; Chung et al. 2022). In such cases, an HFS is observed

toward each edge of the EDC filament. In the HFS, filaments are identified with a large aspect ratio (i.e., filament's length/filament's width, $A > 5$; André et al. 2010) compared to the hub region (< 3). This strongly suggests the onset of the range of star formation processes within a single filamentary cloud and their connection. In addition to these two highlighted configurations, observational evidence for the twisting/coupling of filaments (or intertwined filaments) has only been reported in a couple of SFRs (e.g., NGC 6334 filament; Shimajiri et al. 2019; Lynds Bright Nebulae; Dewangan et al. 2021). However, the simultaneous signature of the HFSs, EDC, and twisted/intertwined filaments in a single SFR has not yet been observed. At present, we do not know if any connection/association exists between these three observational configurations of filaments (i.e., HFSs, EDC, and twisted nature), which is essential to understanding the formation of YSOs and massive stars. In this context, the target of this work is the IC 5146 dark streamer, which is a nearby promising site ($d \sim 600$ pc) to search for different observational configurations of filaments.

This paper focuses on the IC 5146 dark streamer/northern streamer/filamentary structure, which is one of the densest molecular clouds in IC 5146 (Herbig & Reipurth 2008; Roy et al. 2011; Arzoumanian et al. 2013; Chung et al. 2021). The Cocoon Nebula and the northern streamer have been reported as the two main components of IC 5146 in the constellation Cygnus. Using near-IR data, an extinction map of IC 5146 was



Original content from this work may be used under the terms of the [Creative Commons Attribution 4.0 licence](https://creativecommons.org/licenses/by/4.0/). Any further distribution of this work must maintain attribution to the author(s) and the title of the work, journal citation and DOI.

produced by Lada et al. (1994). Embedded dust clumps, filaments, and signposts of star formation activities (i.e., YSOs and outflows) have been reported toward the Cocoon Nebula and the northern streamer (Harvey et al. 2008; Herbig & Reipurth 2008; Arzoumanian et al. 2011, 2019; Johnstone et al. 2017; Zhang et al. 2020). Chung et al. (2021) explored several molecular lines (i.e., ^{13}CO , C^{18}O , N_2H^+ , HCO^+ , CS , SO , NH_2D , and H^{13}CO^+) toward IC 5146 using the Taeduk Radio Astronomy Observatory (TRAO) 14 m telescope, and examined filaments and dense cores in IC 5146 (see also Dobashi et al. 1993; Lada et al. 1994). The clouds associated with the Cocoon Nebula and the streamer were traced in velocity ranges of [6, 9] and [1, 7] km s^{-1} , respectively (Chung et al. 2021). Using Gaia measurements, Wang et al. (2020b) reported distance estimates of 800 ± 100 pc and 600 ± 100 pc for the Cocoon and the streamer, respectively. Based on earlier reported works, the Cocoon Nebula and the northern streamer can be treated as two distinct sources (e.g., Chung et al. 2021).

Dust continuum maps revealed the long filamentary morphology of the IC 5146 dark streamer (Kramer et al. 2003), and two prominent HFSs were investigated toward the eastern and the western parts (i.e., E-HFS and W-HFS) of the streamer (e.g., Arzoumanian et al. 2011, 2019; Roy et al. 2011; Johnstone et al. 2017; Wang et al. 2017, 2019, 2020b; Chung et al. 2021, 2022). Several polarimetry studies were conducted toward the IC 5146 dark streamer (Wang et al. 2017, 2019, 2020b; Chung et al. 2022), which allowed for the exploration of magnetic field structures. These earlier works showed the presence of uniform magnetic field vectors perpendicular to the dark streamer. In general, recent Planck observations (Planck Collaboration et al. 2016a) showed that the low column density filaments (striations; $N_{\text{H}} < 10^{21.7} \text{ cm}^{-2}$) are parallel to the Galactic magnetic field, whereas the magnetic field is perpendicular to filaments with higher column density ($N_{\text{H}} > 10^{21.7} \text{ cm}^{-2}$). These observations are consistent with the theoretical outcomes stating that the magnetic field supports the filament against collapsing into its longer axis and guides the gravity-driven gas contraction (e.g., Nakamura & Li 2008; Inutsuka et al. 2015). A curved magnetic field morphology was investigated toward both ends of IC 5146 (Wang et al. 2019; Chung et al. 2022), and was proposed to be an indication of the EDC process in long filaments. However, such signature has not yet been assessed in potential and nearby EDC filaments.

Chung et al. (2021) found a supersonic nature of the E-HFS and W-HFS in IC 5146, and suggested a collision process of turbulent converging flows to explain the observed HFSs. Based on the positions of the observed HFSs at the long filament *fl*, the scenarios—edge-driven collapse and accretion flows—were proposed to be occurring in the streamer (see Figure 9 in Chung et al. 2022). However, a careful and thorough investigation of the collision process has yet to be done. Furthermore, despite its proximity, the structures in the target site, the IC 5146 streamer, have not been fully investigated. Several other nearby sites have unveiled the presence of multiple sub-filaments and cores as well (e.g., Hacar et al. 2013, 2018). In order to probe various physical processes operating in the streamer, we have carefully examined the dust continuum maps from the Herschel Gould Belt Survey (HGBS; e.g., André et al. 2010; Arzoumanian et al. 2011, 2019), and the velocity structures using the published TRAO ^{13}CO and C^{18}O line data. We have also

employed the *getsf-hires* algorithm (Men’shchikov 2021) to produce high-resolution column density and temperature maps (resolution $\sim 13''$).

The various observational data sets used in this work are presented in Section 2. The derived observational findings are reported in Section 3. Section 4 provides a discussion of our observed outcomes. Finally, Section 5 presents a summary of the major findings of this study.

2. Darta Sets and Analysis

In this paper, we selected an area of $\sim 0^\circ 746 \times 0^\circ 464$ (central coordinates: $l = 93^\circ 659$; $b = -4^\circ 419$) around the IC 5146 dark streamer. The positions of YSOs (i.e., Class I, flat spectrum, and Class II) were collected from Harvey et al. (2008). The published TRAO ^{13}CO (1–0) and C^{18}O (1–0) line data (resolution $\sim 49''$; Chung et al. 2021) were utilized in this work. This paper also uses an integrated C^{18}O (3–2) map obtained from the James Clerk Maxwell Telescope (JCMT; proposal ID: M06BGT02; rest frequency = 329.3305453 GHz). The C^{18}O (3–2) map was downloaded from the JCMT Science Archive/Canadian Astronomy Data Center (CADC), which is a pipeline product (with a pixel scale $\sim 7''.3$ and resolution $\sim 14''$) and was observed in the scan (raster) mode using the Heterodyne Array Receiver Program/Auto-Correlation Spectral Imaging System (HARP/ACSIS; Buckle et al. 2009) spectral imaging system to cover a larger area of the streamer.

The HGBS images at 70–500 μm and the filament skeletons (e.g., Arzoumanian et al. 2011, 2019) were downloaded from the HGBS archive. The NRAO VLA Sky Survey (NVSS; resolution $\sim 45''$; $1\sigma \sim 0.45 \text{ mJy beam}^{-1}$; Condon et al. 1998) 1.4 GHz radio continuum map and the Planck submillimeter map at 353 GHz or 850 μm (resolution $\sim 294''$; Planck Collaboration et al. 2014) were also utilized.

We produced the Herschel H_2 column density and dust temperature maps at different resolutions (i.e., $13''$, $18''$, $24''$, and $36''$) using the *getsf-hires* method described in Men’shchikov (2021). The *getsf* utilities (e.g., *modfits* and *resample*; Men’shchikov 2021) were used in the analysis. The utility *modfits* was used to convert the Herschel flux densities at 70 and 160 μm from units of jansky per pixel to megajansky per steradian, while the utility *resample* was utilized to regrid all the Herschel images at 70–500 μm to the pixel scale of the image at 70 μm (i.e., $3''$). Thereafter, images with different possible resolutions (i.e., $8''$, $13''$, $18''$, $24''$, and $36''$) were generated, and the final spectral fitting was performed (excluding the image at 70 μm) to generate high-resolution column density and temperature maps. The Herschel 70 μm image is generally not used in the spectral fitting due to the contamination caused by warm emission originating from UV-heated dust (e.g., polycyclic aromatic hydrocarbons or transiently heated small dust grains), thus leading to overestimation of the dust temperature (i.e., underestimation of column density). However, even excluding the 70 μm continuum image in the spectral fitting, *getsf-hires* can still produce images with a resolution of $8''$ (i.e., the resolution of the image at 70 μm ; see Men’shchikov 2021, for more details). Our high-resolution column density and temperature maps at the resolution of the 70 μm continuum image are noisy, possibly because of insignificant features present in the image at 70 μm . Therefore, in this paper, we have utilized the column density

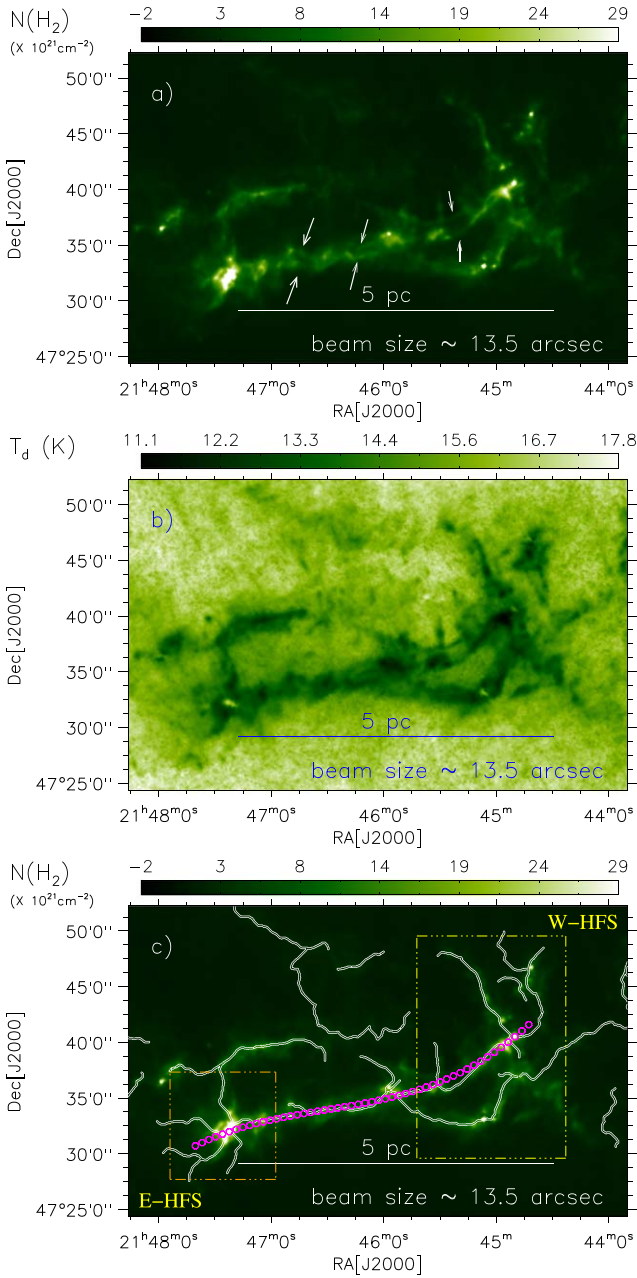


Figure 1. Panel (a) shows a Herschel column density map (resolution $\sim 13''$) of an area containing the IC 5146 dark streamer (size $\sim 0^\circ 746 \times 0^\circ 464$). Different sub-filaments are indicated by arrows. Panel (b) presents the Herschel temperature map (resolution $\sim 13''$). (c) Same as Figure 1(a), but it shows the Herschel filament skeletons (see white curves from Arzoumanian et al. 2019) and several small circular regions (in magenta; radii = $25''$) along the filamentary structure. Two dotted-dashed boxes indicate the locations of the HFSs, which are labeled E-HFS and W-HFS. A scale bar corresponding to 5 pc (at a distance of 600 pc) is shown in each panel.

and temperature maps at resolutions of $\sim 13''$, $18''$, $24''$, and $36''$.

3. Results

In this section, we present the results derived using a careful analysis of the Herschel data and the molecular line data, which have enabled us to uncover new insights into the physical processes operating in the IC 5146 dark streamer.

3.1. Signatures of Two Intertwined Sub-filaments in the IC 5146 Dark Streamer

Figures 1(a) and (b) display the Herschel column density ($N(\text{H}_2)$) and temperature (T_d) maps (resolution $\sim 13''$) of our selected target area around the IC 5146 dark streamer. For the first time, we present these high-resolution maps of our target site, which have been produced using the *getsf-hires* method as discussed in Section 2. Visual inspection of the column density map shows several extended structures. Two previously reported HFSs (i.e., E-HFS and W-HFS) and filament skeletons are also shown in the Herschel column density map (see Figure 1(c)), which were identified using the HGBS column density map at the resolution of $\sim 18''$ (e.g., Arzoumanian et al. 2019). In earlier works, a single long filament, designated as *fl*, hosting E-HFS and W-HFS at its opposite ends was mainly discussed. We have also marked several small circular regions (radii = $25''$) along this long filament (see magenta circles in Figure 1(c)), where some physical parameters (such as column density, temperature etc.) are determined (see Section 3.3). In this paper, the Herschel column density map at the resolution of $\sim 13''$ reveals the presence of two intertwined sub-filaments (i.e., *fl-A* and *fl-B*; $T_d \sim 11\text{--}15$ K), which are indicated by arrows in Figure 1(a). We have considered the long filament *fl* as the main filament, which appears to be composed of two intertwined substructures. This is a new result found in the IC 5146 dark streamer. The implication of this outcome is discussed in Section 4.2.

Figure 2(a) shows the boundaries of different structures traced in the column density map. In order to identify these structures, we used the $N(\text{H}_2)$ contour at $5.22 \times 10^{21} \text{ cm}^{-2}$ and the IDL-based *clumpfind* algorithm (Williams et al. 1994). The *clumpfind* algorithm divides two- and three-dimensional data into distinct emission clumps by contouring data with a multiple of the rms noise (see more information in Williams et al. 1994). The identified structures primarily trace the eastern filament and the western HFS. We have also identified several clumps toward the structures as presented in Figure 2(a). We used the $N(\text{H}_2)$ contours at $[5.22, 9.3, \text{ and } 12] \times 10^{21} \text{ cm}^{-2}$ to trace these clumps. In the $N(\text{H}_2)$ map, we define the clumps as non-filamentary arbitrarily shaped structures (size ~ 0.5 pc), while the cores are circular-shaped structures (size ≤ 0.1 pc; see Section 3.2). In standard terminology, the clumps have a lower density ($\sim 10^4 \text{ cm}^{-3}$) than the embedded cores ($> 10^5 \text{ cm}^{-3}$; Onishi et al. 2002; Saito et al. 2006). The locations and boundaries of the clumps are displayed in Figure 2(b). Filled inverted triangles show the clumps distributed toward the long filament *fl*, while the clumps located away from this structure are highlighted by open inverted triangles. Figure 2(c) displays the distribution of the Herschel clumps, the ionized emission traced by the NVSS 1.4 GHz continuum contour, and the Planck 353 GHz or $850 \mu\text{m}$ continuum emission against the structures as presented in Figure 2(a). We do not find any noticeable radio continuum emission toward the long filament *fl*, including both the HFSs. The elongated appearance is also evident in the Planck 353 GHz or $850 \mu\text{m}$ continuum map, which does not show any inner structures due to its coarse beam size.

We have also computed the mass of each Herschel clump using the equation, $M_{\text{clump}} = \mu_{\text{H}_2} m_H A_{\text{pix}} \Sigma N(\text{H}_2)$, where μ_{H_2} is the mean molecular weight per hydrogen molecule (i.e., 2.8), A_{pix} is the area subtended by one pixel (i.e., $3'' \text{ pixel}^{-1}$), and

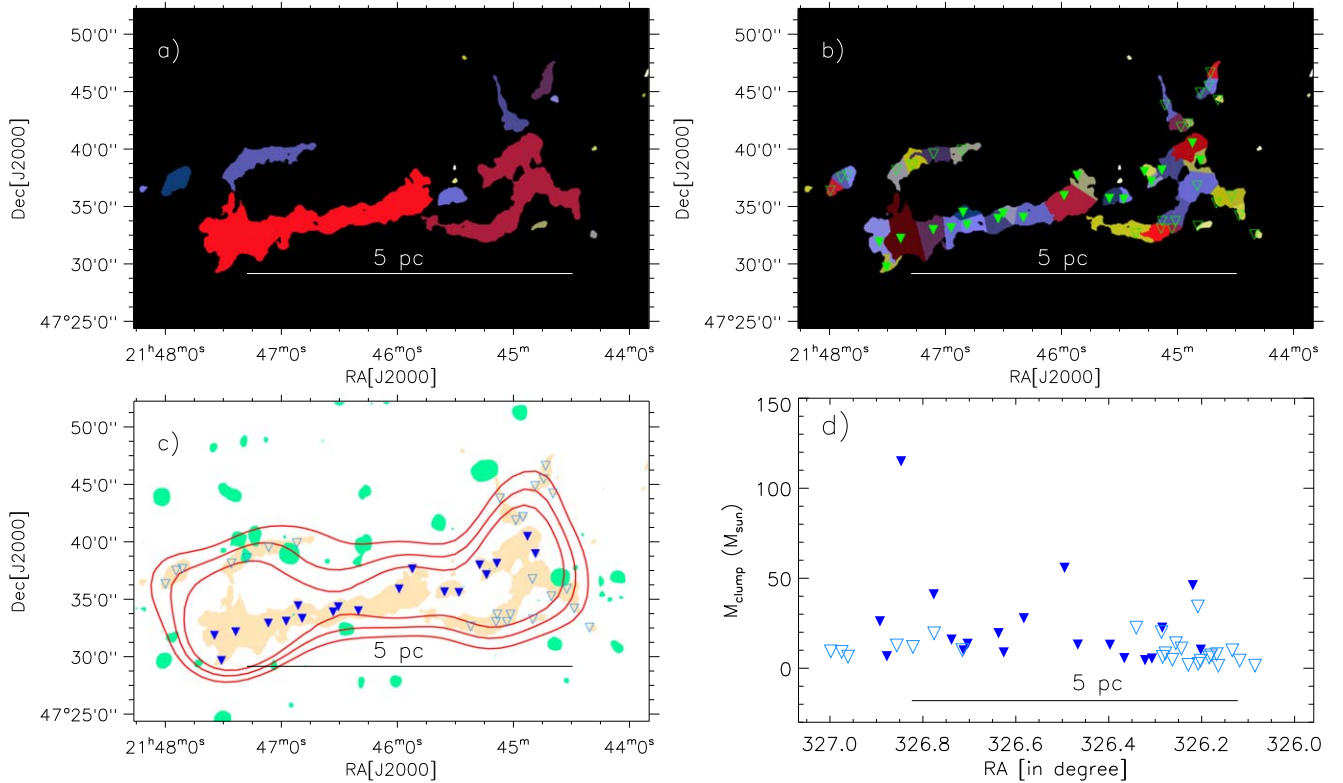


Figure 2. (a) Several structures are presented and are depicted in the column density map at a contour level of $5.22 \times 10^{21} \text{ cm}^{-2}$. (b) Spatial distribution of clumps identified toward the structures shown in Figure 2(a). The positions of these clumps are indicated by filled and open inverted triangles. The boundary of each Herschel clump is also shown. Clumps highlighted by filled symbols are selected toward the elongated structure (see Figure 1(c)), while open symbols present clumps located away from the elongated structure. Panel (c) shows a filled $N(\text{H}_2)$ contour (in moccasin) at $5.22 \times 10^{21} \text{ cm}^{-2}$, a filled NVSS 1.4 GHz continuum contour (in spring green), and the emission contours at [4.92, 5.70, 6.42] MJy sr^{-1} from the Planck 353 GHz or $850 \mu\text{m}$ intensity map. Inverted triangles are the same as shown in Figure 2(b). Panel (d) shows a variation of clump masses against their corresponding longitudes (see filled and open inverted triangles in Figure 2(b)). A scale bar corresponding to 5 pc (at a distance of 600 pc) is shown in each panel.

$\Sigma N(\text{H}_2)$ is the total column density (see also Dewangan et al. 2017). Figure 2(d) presents the mass distribution against the position of all the clumps, allowing us to examine the mass distribution of clumps. Filled symbols show the clumps distributed toward the long filament *fl*, and massive ones appear to be present at its opposite ends.

In order to highlight two sub-filaments, a false color map is produced using the Herschel image at $250 \mu\text{m}$ (see Figure 3(a)). Previously reported positions of the Class I YSOs, flat-spectrum sources, and Class II YSOs (from Harvey et al. 2008) are shown in the Herschel image. We also employed the “Edge-DoG” algorithm on the Herschel image at $250 \mu\text{m}$, and its outcome is presented in Figure 3(b). The IDL-based Edge-DoG filter enhances the extended brightness inhomogeneities (e.g., sharp edges) based on the difference in Gaussian filter techniques (Assirati et al. 2014). The positions of HFSs (i.e., E-HFS and W-HFS) and two possible sub-filaments are marked in Figure 3(b). Figure 3(c) exhibits a zoom-in view of the Herschel column density map toward the IC 5146 dark streamer, where the two sub-filaments *fl-A* and *fl-B* are indicated by arrows. Based on a visual inspection of Herschel images, we have presented a cartoon diagram displaying the possible configuration of *fl-A* and *fl-B* in Figure 3(d). The overlapping areas of the sub-filaments are shown by filled hexagons, where either the YSOs or dense sources are identified. The implication of this configuration is discussed in Section 4.2.

3.2. Identification of Filament Skeletons and the Dust Continuum Sources/Cores on $N(\text{H}_2)$ Map at $13''.5$

To identify the dust continuum sources (or cores) and filament skeletons present in our target site IC 5146 streamer, we used the *getsf* tool presented in Men’shchikov (2021). The *getsf* method is capable of extracting the sources and filaments from an astronomical image and requires only a single user input of the maximum size of the structure to extract. We employed the *getsf* utility on the $N(\text{H}_2)$ map at $13''.5$. The maximum source and filament size were set to be $20''$ and $200''$, respectively. Figure 4(a) presents the overlay of *getsf* extracted sources on the $N(\text{H}_2)$ map. The size of sources indicates their footprint size, which is plotted by their estimated major and minor axes. We have only selected the sources that lie within the $N(\text{H}_2)$ contour value of $5.22 \times 10^{21} \text{ cm}^{-2}$. A total of 67 sources were found and are displayed in Figure 4. The overlay of filament skeletons on the $N(\text{H}_2)$ map at the spatial scale of $\sim 14''$ is shown in Figure 4(b). The presence of at least two close filaments along the major axis of *fl* is marked by arrows. We have overlaid the *getsf* sources on the image. The size of the dots is proportional to the footprint area of *getsf* sources. The color scheme of the sources infers their mass distribution. The mass of the sources is estimated by the same method presented in Section 3.1. This analysis suggests that the more massive cores are located at the hub locations (i.e., E-HFS and W-HFS) compared to the other areas. We cleaned the *getsf* identified filament skeletons by removing the spurious structures and the structures outside of our target region.

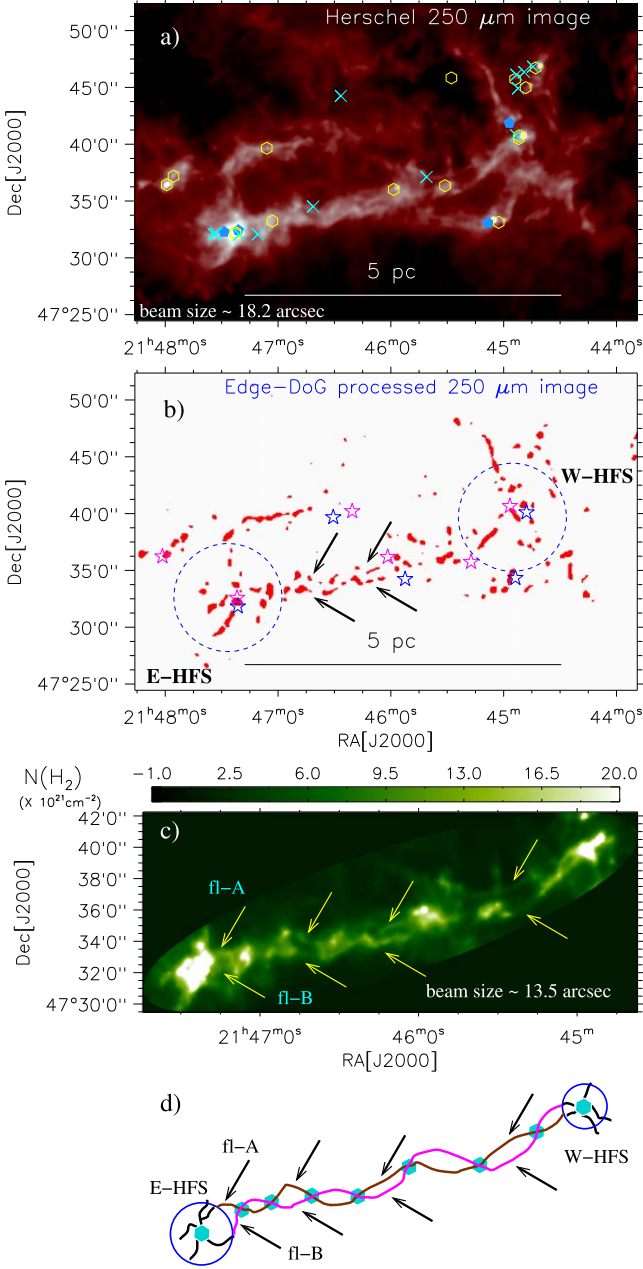


Figure 3. (a) Overlay of the positions of YSOs (Harvey et al. 2008) on the Herschel image at 250 μm . Hexagons, filled pentagons, and multiplication signs represent Class I YSOs, flat-spectrum sources, and Class II YSOs, respectively. Panel (b) shows the Herschel image at 250 μm , which has been exposed to the Edge-DoG algorithm. Two sub-filaments and two HFSs (i.e., E-HFS and W-HFS) are indicated by arrows and dashed circles, respectively. Blue stars and magenta stars represent the blueshifted and redshifted outflow lobes (from Zhang et al. 2020), respectively. Panel (c) presents a zoom-in view of the Herschel column density map (resolution $\sim 13''$) toward the IC 5146 dark streamer. A scale bar corresponding to 5 pc (at a distance of 600 pc) is shown in panels (a) and (b). (d) A cartoon displaying the positions of E-HFS, W-HFS, and the possible distribution of intertwined filaments fl-A and fl-B. Filled hexagons signify the overlapping areas of fl-A and fl-B.

3.3. Kinematics of Molecular Gas

3.3.1. Variation of Radial Velocity and Mach Number Along the Filament fl

We have reexamined the published TRAO ^{13}CO and C^{18}O line data (effective beam size $\sim 49''$; Chung et al. 2021) toward

the IC 5146 dark streamer. Figures 5(a) and (b) display the integrated intensity (i.e., moment-0) maps of $^{13}\text{CO}(J=1-0)$ and $\text{C}^{18}\text{O}(J=1-0)$ emission over velocity ranges of [0.8, 6] and [1.0, 5.5] km s^{-1} , respectively. The distribution of both molecular emissions seems to closely follow the long filament fl, but the two sub-filaments (i.e., fl-A and fl-B) are not spatially resolved in the molecular maps due to their coarse beam sizes. Both molecular emissions are more intense toward the HFSs (i.e., E-HFS and W-HFS).

In Figure 6(a), we show the distribution of Herschel clumps, YSOs (from Harvey et al. 2008), and outflow lobes (from Zhang et al. 2020) toward the IC 5146 dark streamer. We also mark open circles to highlight the positions of several circular regions along the long filament fl (see also Figure 1). Average column density and average dust temperature are computed for each circular region using the Herschel column density and temperature maps at different resolutions (i.e., $13''$, $18''$, $24''$, and $36''$), respectively. With the help of these values, Figures 6(b) and (c) display the column density profile and the dust temperature profile along the filamentary structure, respectively. We find the column density peaks at the ends of the long filament fl, and the presence of cold dust emission ($T_d \sim 11-15$ K) toward the filament fl. These outcomes are consistent in all the Herschel column density and temperature maps at different resolutions.

We also produced average spectra of ^{13}CO and C^{18}O toward each circular region, enabling us to determine the mean velocity (V_{lsr}) and the FWHM line width (ΔV) of each spectrum. The V_{lsr} and ΔV are estimated by Gaussian fitting of each averaged spectrum. In Figures 6(d) and (e), we present the ^{13}CO and C^{18}O velocity profiles and the ^{13}CO and C^{18}O line width profiles along the filamentary structure, respectively. The variation in V_{lsr} and ΔV along the filament can be seen. In other words, there is a hint of velocity oscillation along the filament. The knowledge of the line width value is also used to compute the nonthermal velocity dispersion, Mach number, and ratio of thermal to nonthermal pressure toward each circular region. Mach number is defined as the ratio of nonthermal velocity dispersion (σ_{NT}) to the speed of sound (c_s). The speed of sound $c_s = (kT_{\text{kin}}/\mu m_{\text{H}})^{1/2}$ can be estimated using the value of gas kinetic temperature (T_{kin}) and mean molecular weight ($\mu = 2.37$; approximately 70% H and 28% He by mass). Here, we used the average dust temperature instead of T_{kin} , which has been estimated to be ~ 14.2 K from the Herschel temperature map. Based on the recommendations of Lada et al. (2003), we computed the ratio of thermal to nonthermal (or turbulent) pressure (i.e., $R_p = c_s^2/\sigma_{\text{NT}}^2$). The nonthermal velocity dispersion can be determined using the following equation:

$$\sigma_{\text{NT}} = \sqrt{\frac{\Delta V^2}{8 \ln 2} - \sigma_{\text{T}}^2}, \quad (1)$$

where ΔV is defined earlier, $\sigma_{\text{T}} = (kT_{\text{kin}}/30m_{\text{H}})^{1/2}$ for C^{18}O and $=(kT_{\text{kin}}/29m_{\text{H}})^{1/2}$ for ^{13}CO is the thermal broadening at T_{kin} (or $T_d \sim 14.2$ K). Figures 6(f)–(h) display the variation in the nonthermal velocity dispersion, Mach number, and ratio of thermal to nonthermal gas pressure for ^{13}CO and C^{18}O along the filamentary structure, respectively. Using the ^{13}CO and C^{18}O emissions, the Mach number is found to be larger than 1, and the low ratios of thermal to nonthermal pressure (< 1) are evident for

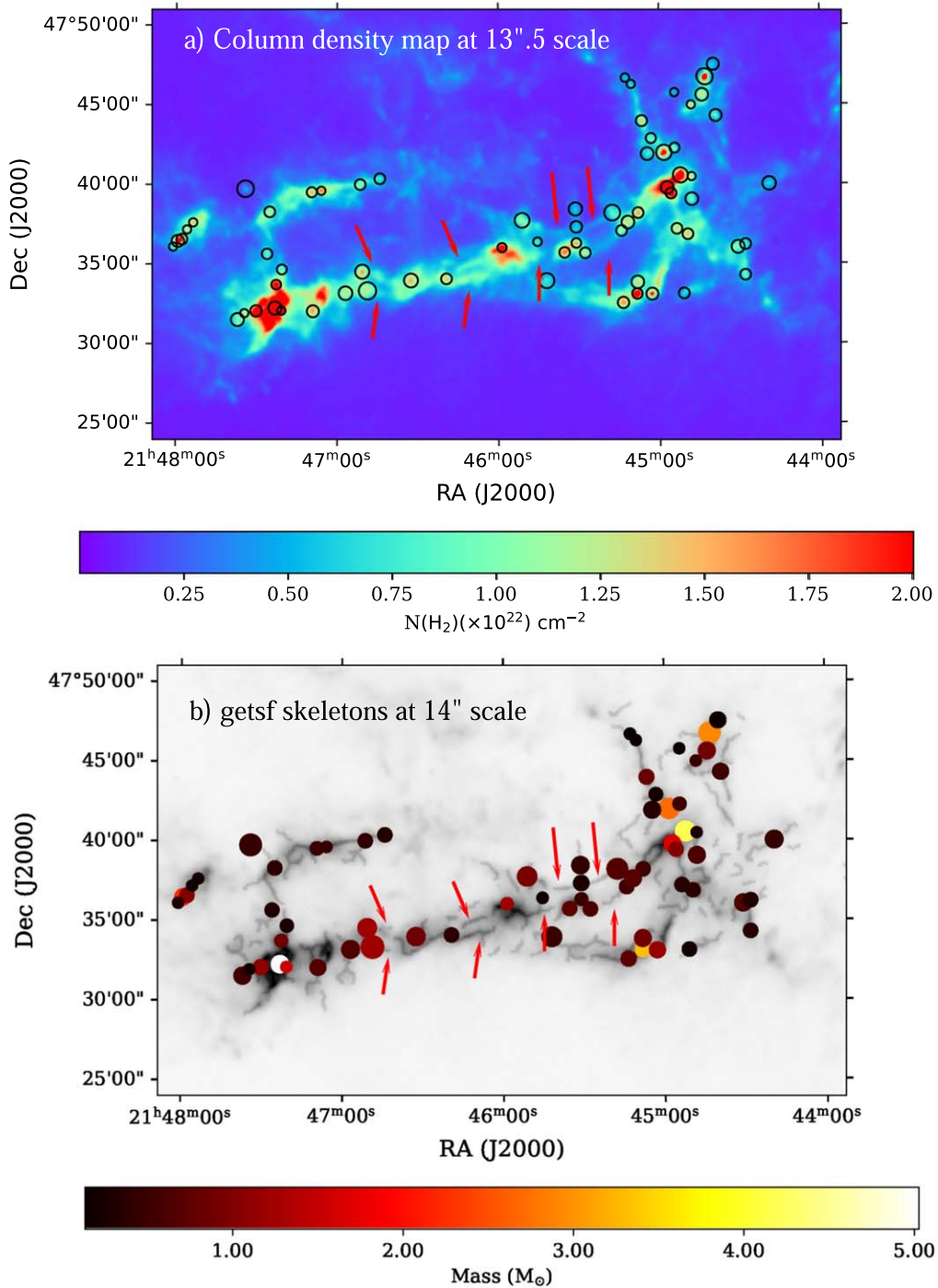


Figure 4. (a) H_2 column density ($N(\text{H}_2)$) map at $13''.5$ resolution. The getsf extracted sources are overlaid and shown by their footprint size (see the text for more details). (b) Overlay of the getsf identified skeletons at $14''$ scale on the $13''.5$ $N(\text{H}_2)$ map. The size of dots is proportional to the footprint area of getsf sources. The arrows mark the sub-filaments $fl-A$ and $fl-B$ (see Figure 3).

all the selected circular regions. It implies the presence of supersonic and nonthermal motion in the filamentary structure. Furthermore, higher values of $N(\text{H}_2)$, Mach number, and lower values of R_p are found toward the central hub of the E-HFS compared to the other HFS (i.e., W-HFS).

3.3.2. Signatures of Two Velocity Components toward the Filament fl

We have examined the position–velocity (p – v) diagrams of the ^{13}CO and C^{18}O emissions along several lines passing through the shorter axis of fl . In this paper, we have only

presented the p – v diagrams along four arrows $p1$ – $p4$ (see Figure 5(b)). One can notice that the paths/arrows $p1$ and $p4$ pass through HFS-W and HFS-E, respectively. The p – v diagrams of ^{13}CO along $p1$ – $p4$ are presented in Figures 7(a), (c), (e), and (g), respectively. Figures 7(b), (d), (f), and (h) present p – v diagrams of C^{18}O along $p1$ – $p4$, respectively. In the direction of both HFSS, p – v diagrams hint at the presence of two velocity components around 2 and 4 km s^{-1} , which are connected in the velocity space. We have also studied the velocity channel maps of the ^{13}CO emission (not shown in this paper), supporting the existence of two velocity components

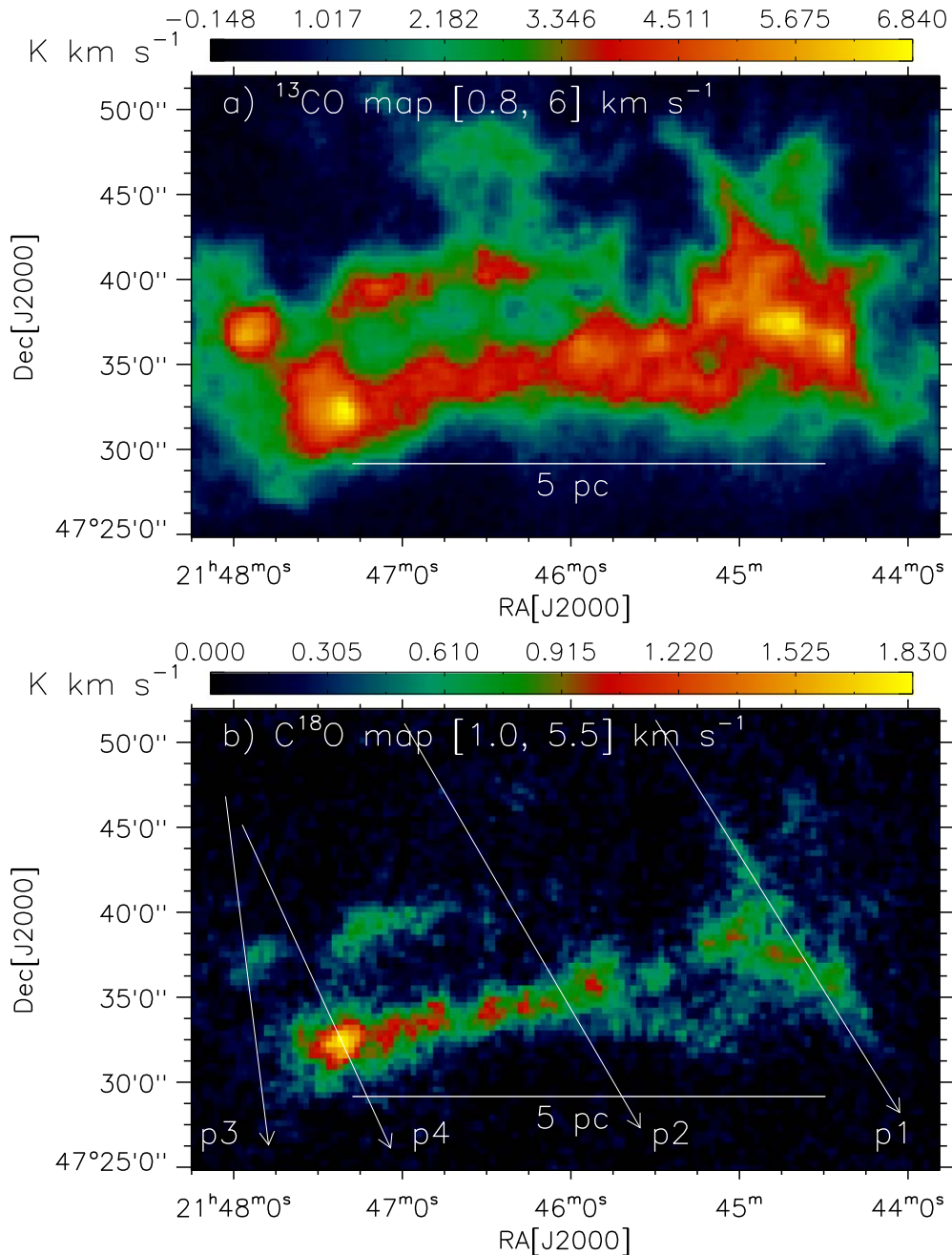


Figure 5. TRAO-integrated intensity (or moment-0) maps of (a) ^{13}CO and (b) C^{18}O toward the IC 5146 dark streamer. The molecular emission is integrated over a velocity interval, which is given in each panel (in kilometers per second). In panel (b), four arrows (p1–p4) are indicated, and p - v diagrams along these paths are presented in Figure 7. A scale bar corresponding to 5 pc (at a distance of 600 pc) is shown in each panel.

(i.e., [1, 2] and [3, 4] km s^{-1}). In this context, we show the intensity-weighted mean velocity (i.e., moment-1) maps of ^{13}CO and C^{18}O emission in Figures 8(a) and (b), respectively.

Based on a careful examination of the molecular line data, we have produced integrated intensity maps for two different velocity ranges (see Figures 8(c) and (d)). ^{13}CO emission maps at [0.8, 2.5] and [3, 6] km s^{-1} , and the C^{18}O emission maps at [1, 2.5] and [3, 6] km s^{-1} have been generated (see Figures 8(c) and (d)). Figures 8(e) and (f) display the intensity-weighted velocity dispersion (i.e., moment-2) maps of ^{13}CO and C^{18}O emission, respectively. In Figure 8(c), we find the overlapping zones of the two cloud components, where both the HFSs and the central part of the long filament f_l are depicted spatially (see

also the C^{18}O emission in Figure 8(d)). In these locations, higher velocity dispersions are also found, inferring the presence of either multiple velocity components (see Figure 8(c), (e)) or the presence of nonthermal gas motions (see Figure 8(d), (f)). Together, the molecular line data support the physical connection of the two cloud components (around 2 and 4 km s^{-1}) in both physical and velocity space.

3.3.3. Existence of Two Intertwined Molecular Filaments toward the Filament f_l ?

The cloud component at [3, 6] km s^{-1} (or around 4 km s^{-1}) traced using both the molecular lines has an elongated

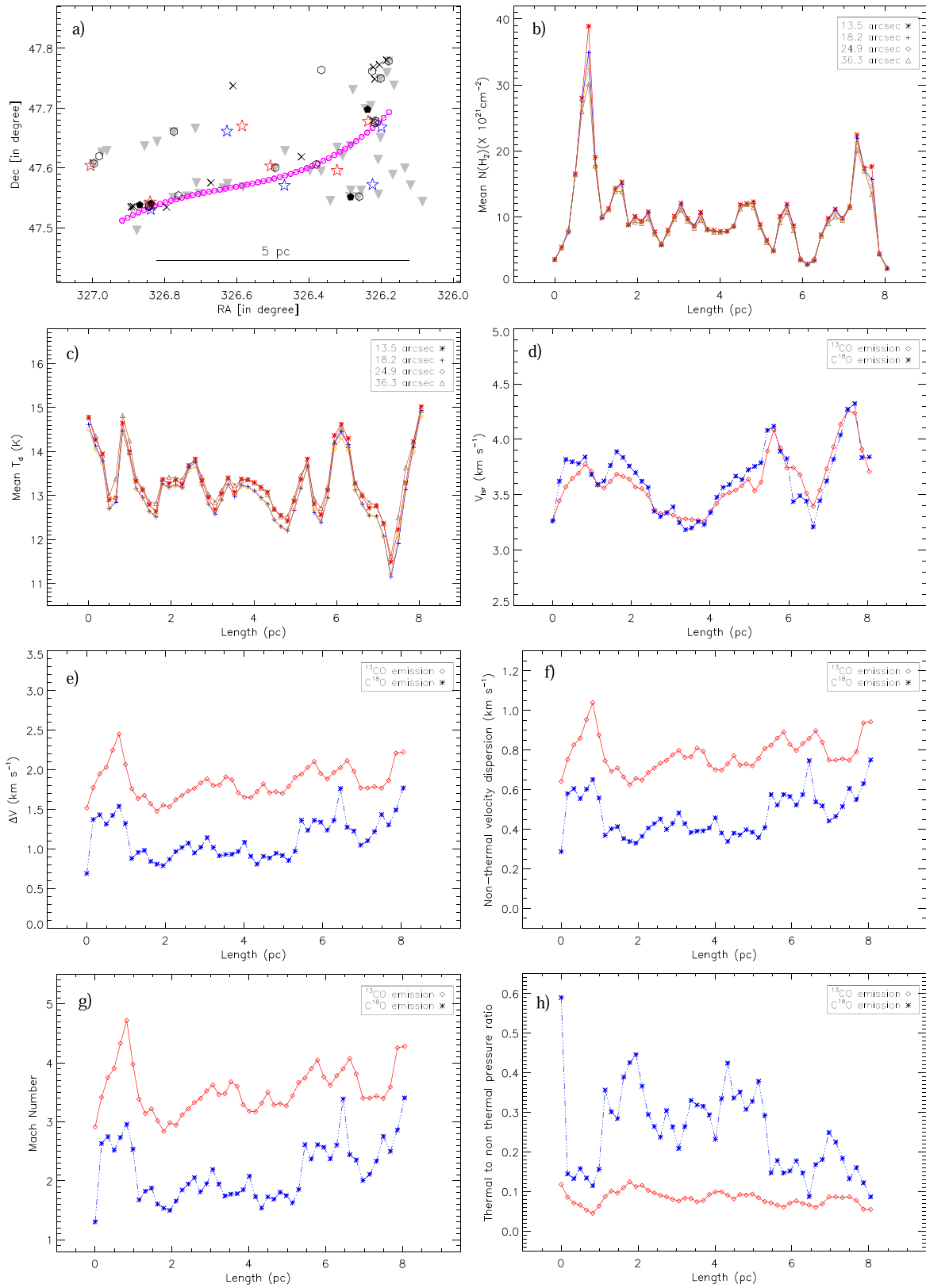


Figure 6. Panel (a) presents the distribution of Herschel clumps (filled inverted triangles), infrared excess sources (i.e., Class I YSOs (hexagons), flat-spectrum sources (filled pentagons), and Class II YSOs (multiplication signs), from Harvey et al. (2008), and outflow lobes (stars; from Zhang et al. 2020, see also Figure 2 and 3). Open circles (in magenta) represent the positions of several selected regions along the filamentary structure (see also Figure 1(c)), where average molecular spectra, average column densities, and average dust temperatures are computed. Panels (b)–(f) display the variation in the column density, dust temperature, radial velocity, FWHM line width, nonthermal velocity dispersion, Mach number, and the ratio of thermal to nonthermal gas pressure along the filamentary structure highlighted in Figure 6(a). In the direction of each circle marked in Figure 6(a), the values of dust temperature and column density are computed from the Herschel temperature and column density maps having different resolutions, while other physical parameters are extracted using the ^{13}CO and C^{18}O line data.

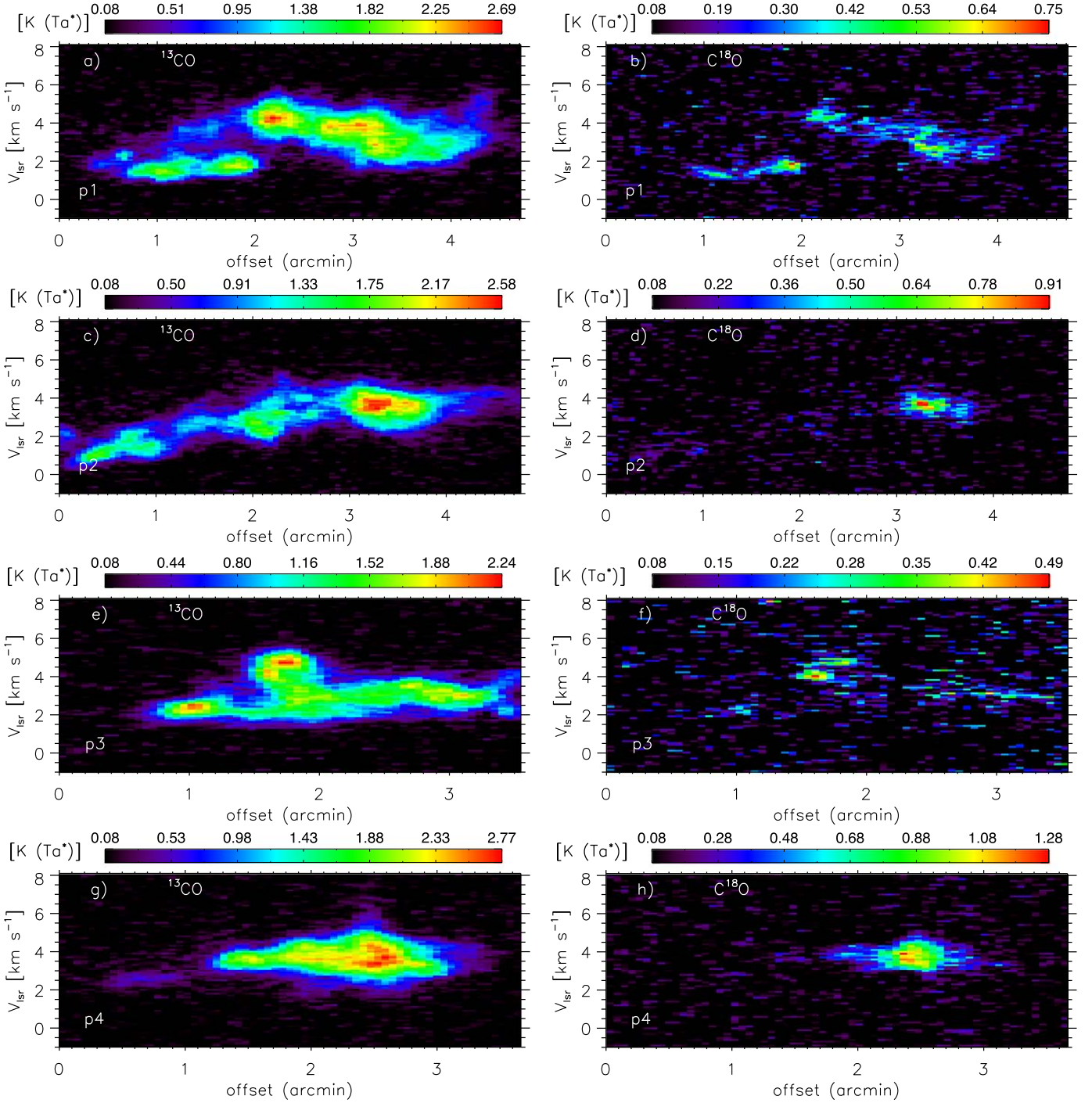


Figure 7. Left column, panels (a), (c), (e), and (g): p - v diagrams of ^{13}CO along the four arrows p1–p4. Right column, panels (b), (d), (f), and (g): p - v diagrams of C^{18}O along the four arrows p1–p4. Arrows p1–p4 are indicated in Figure 5(b).

appearance similar to the long filament fl , while the second component around 2 km s^{-1} does not show any elongated morphology like fl (see Figure 8(d)). The previously reported N-filament (see Figure 8(d) in this paper and Figure 2 in Chung et al. 2022) toward the western end of the fl is associated with the cloud around 2 km s^{-1} . Concerning the cloud component around 4 km s^{-1} , Figure 9(a) shows the moment-1 map of the C^{18}O emission, revealing the presence of velocity variations along the filamentary feature. To further infer velocity variations, using the moment-1 maps of ^{13}CO and C^{18}O , we extracted the velocity profiles along the arrow highlighted in

Figure 9(a) (see Figure 9(b)). A velocity variation/oscillation is traced in both molecular emissions. In the direction of the eastern and central parts of the IC 5146 dark streamer, the Herschel image at $250 \mu\text{m}$ and the integrated JCMT C^{18}O (3–2) map are presented in Figures 9(c) and (d), respectively. Due to the limited sensitivity, the existing JCMT C^{18}O (3–2) map could only hint at the existence of two intertwined molecular filaments (see the arrows in Figure 9(d)) as investigated in the Herschel maps (i.e., fl -A and fl -B). For comparison purposes, we also place arrows over the Herschel image at $250 \mu\text{m}$. To further study these molecular filaments,

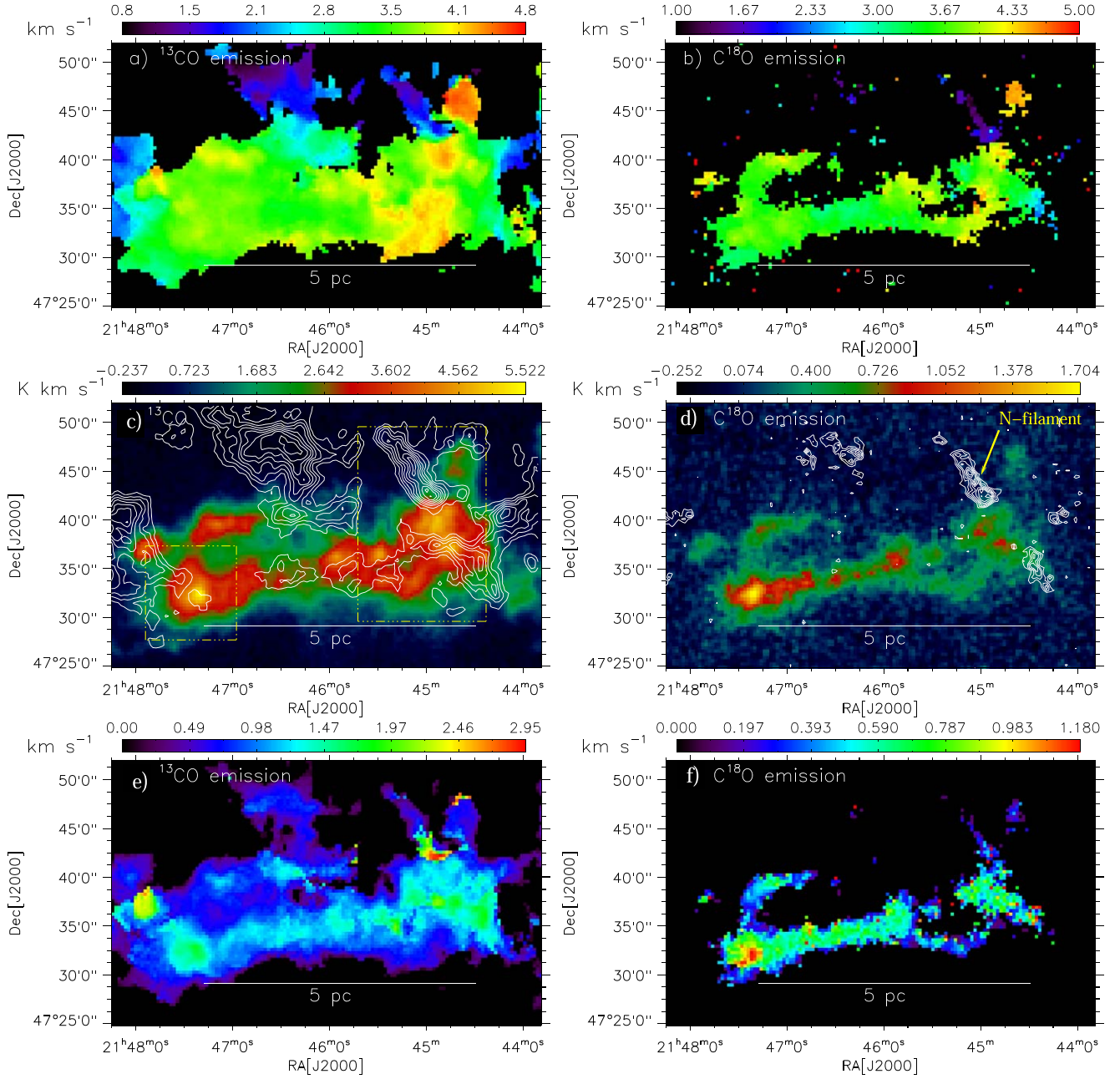


Figure 8. (a) ^{13}CO moment-1 map of our selected target area (Figure 1(a)). (b) C^{18}O moment-1 map. (c) Overlay of the ^{13}CO integrated intensity emission contours at $[0.8, 2.5]$ km s^{-1} on the ^{13}CO integrated intensity map at $[3, 6]$ km s^{-1} . The contour levels are $2.56 \text{ K (in } T_a^*) \text{ km s}^{-1} \times (0.2, 0.3, 0.4, 0.5, 0.6, 0.7, 0.8, 0.9)$. (d) Overlay of the C^{18}O integrated intensity emission contours at $[1, 2.5]$ km s^{-1} on the C^{18}O integrated intensity map at $[3, 6]$ km s^{-1} . The contour levels are $0.45 \text{ K (in } T_a^*) \text{ km s}^{-1} \times (0.3, 0.4, 0.5, 0.6, 0.7, 0.8, 0.9)$. (e) ^{13}CO moment-2 map. (f) C^{18}O moment-2 map. A scale bar corresponding to 5 pc (at a distance of 600 pc) is shown in each panel.

one would need new high-resolution and high-sensitivity molecular line data for a larger area around the IC 5146 dark streamer. We found that the high-resolution C^{18}O maps (resolution $\sim 15''\text{--}20''$) at different transitions (i.e., $J = 1\text{--}0$, $J = 2\text{--}1$, and $J = 3\text{--}2$) of the IC 5146 dark streamer presented in Bell (2008) reveal similar morphology as seen in the Herschel maps. Thus, the continuum and the molecular maps hint at the existence of two intertwined sub-filaments.

4. Discussion

Based on several previously published works, the dark streamer of IC 5146 has been considered as a single and long

filament f_l having an aspect ratio larger than 5 (Arzoumanian et al. 2011, 2019; Johnstone et al. 2017; Wang et al. 2017, 2019, 2020b; Zhang et al. 2020; Chung et al. 2021, 2022), which is also indicated in Figure 1(c). One prominent HFS has been traced toward the east end (E-HFS) and the west end (W-HFS) of the dark streamer (see Figure 1(c)). Chung et al. (2022) presented a cartoon showing the observed configuration of the streamer (see Figure 9 in their paper). In our high-resolution Herschel column density map, both the HFSs are associated with the regions of high column densities (see Figure 6(b)). Noticeable YSOs and outflow lobes (e.g., Harvey et al. 2008; Zhang et al. 2020) have been reported

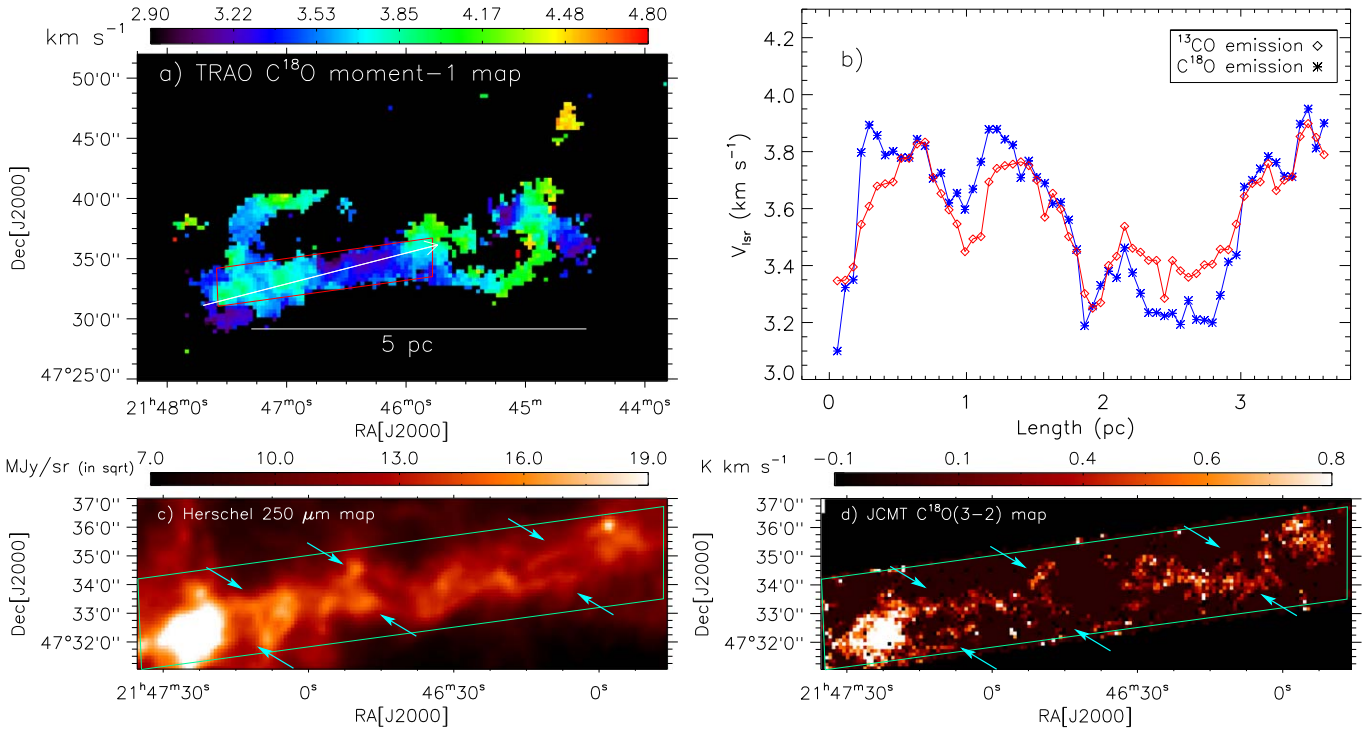


Figure 9. Panel (a) shows the TRAO C^{18}O moment-1 map of our selected target area (Figure 1(a)), which is generated for the molecular cloud at $[2.9, 6] \text{ km s}^{-1}$ (see Figure 8(f)). A scale bar corresponding to 5 pc (at a distance of 600 pc) is presented. Panel (b) displays the variation in radial velocities along an arrow marked in Figure 9(a), which are extracted using the ^{13}CO and C^{18}O moment-1 maps. Panel (c) shows areas toward the eastern and central parts of the IC 5146 dark streamer using the Herschel $250 \mu\text{m}$ image. Panel (d) presents an integrated JCMT C^{18}O (3–2) map. In panels (a), (c), and (d), a solid box highlights the area covered in the JCMT C^{18}O (3–2) map.

toward both the ends of the dark streamer (i.e., E-HFS and W-HFS; see Figure 6(a)), supporting ongoing star formation activities (e.g., Chung et al. 2021, 2022). The absence of radio continuum emission and high column density areas toward the E-HFS and W-HFS hints at the potential sites of future massive star formation (see Figure 2). Earlier published results were interpreted in favor of the edge-driven collapse and fragmentation scenario in the dark streamer (see Wang et al. 2019; Chung et al. 2022, and references therein). Additionally, in support of the proposed edge collapse scenario, the curved B -field morphology in core-scale HFSs toward both ends was detected (see Wang et al. 2019; Chung et al. 2022, and references therein). Apart from the IC 5146 streamer, we have verified this signature in other nearby EDC filaments as well.

4.1. Magnetic Field Orientations in Nearby Candidate EDC Filaments

In the introduction to this paper, we have highlighted the candidate filaments experiencing edge collapse. Apart from the IC 5146 dark streamer ($d \sim 600$ pc), we find three other EDC filaments (i.e., Mon R1 ($d \sim 760$ pc), S242 ($d \sim 2.1$ kpc), and NGC 6334 ($d \sim 1.3$ kpc)), which are nearby EDC filamentary systems ($d \lesssim 2$ kpc). Existing observations of dust-polarized emission from the Planck telescope have been employed to study the large-scale magnetic field of the four EDC filaments. We used the Planck 353 GHz Stokes I , Q , and U maps to estimate the linear polarization angles of polarized dust emission caused by the anisotropic dust grains in our target sites. The Stokes I , Q , and U maps were converted from the cosmic microwave background (CMB) temperature (K_{cmb}) scale to units of megajansky per steradian using the unit

conversion factor of 246.54 (e.g., Planck Collaboration et al. 2016d). We also smoothed the Stokes maps by *astropy*-based Gaussian 2D-kernel (input parameter $x_{\text{stddev}} = 2$) to increase the signal-to-noise ratio. We estimated the polarization angles in Galactic coordinates using the conventional relation of $\theta_{\text{Gal}} = 0.5 \times \arctan 2(-U, Q)$, where $-U$ is used to follow IAU convention (see more details in Planck Collaboration et al. 2015) and a two-argument function $\arctan 2$ is used to avoid the π ambiguity in the estimation of polarization angles. The magnetic field orientations were then computed by adding 90° in the electric field polarization angles (e.g., Planck Collaboration et al. 2016b, 2016c). We term this angle as B_{Gal} throughout the paper, which is measured from Galactic north to east along the counterclockwise direction.

The distribution of the plane of the sky (POS) magnetic field in the direction of our selected EDC filaments IC 5146 dark streamer, S242, Mon R1, and NGC 6334 is displayed by streamlines in Figure 10. We used *streamplot* in *matplotlib* to display the magnetic field orientations toward our selected targets. The magnetic field direction is nearly perpendicular to all the filaments, consistent with observations of other targets (e.g., Palmeirim et al. 2013; Cox et al. 2016; Planck Collaboration et al. 2016a). The ^{13}CO emission at the velocity range of $[0.8, 2.5] \text{ km s}^{-1}$ (see Figure 8(c)) appears to be parallel to the B -field orientation as shown in Figure 10(a). It is reported that faint filaments (striations) are well aligned to the magnetic fields, and the main filament can gain its mass from these striations (e.g., Palmeirim et al. 2013; Zhang et al. 2020). Therefore, the ^{13}CO emissions parallel to the B field show that the IC 5146 dark streamer is not isolated but interacts with the natal clouds. However, interestingly the B -field direction is curved at the edges of our target filaments. As discussed by Wang et al. (2019)

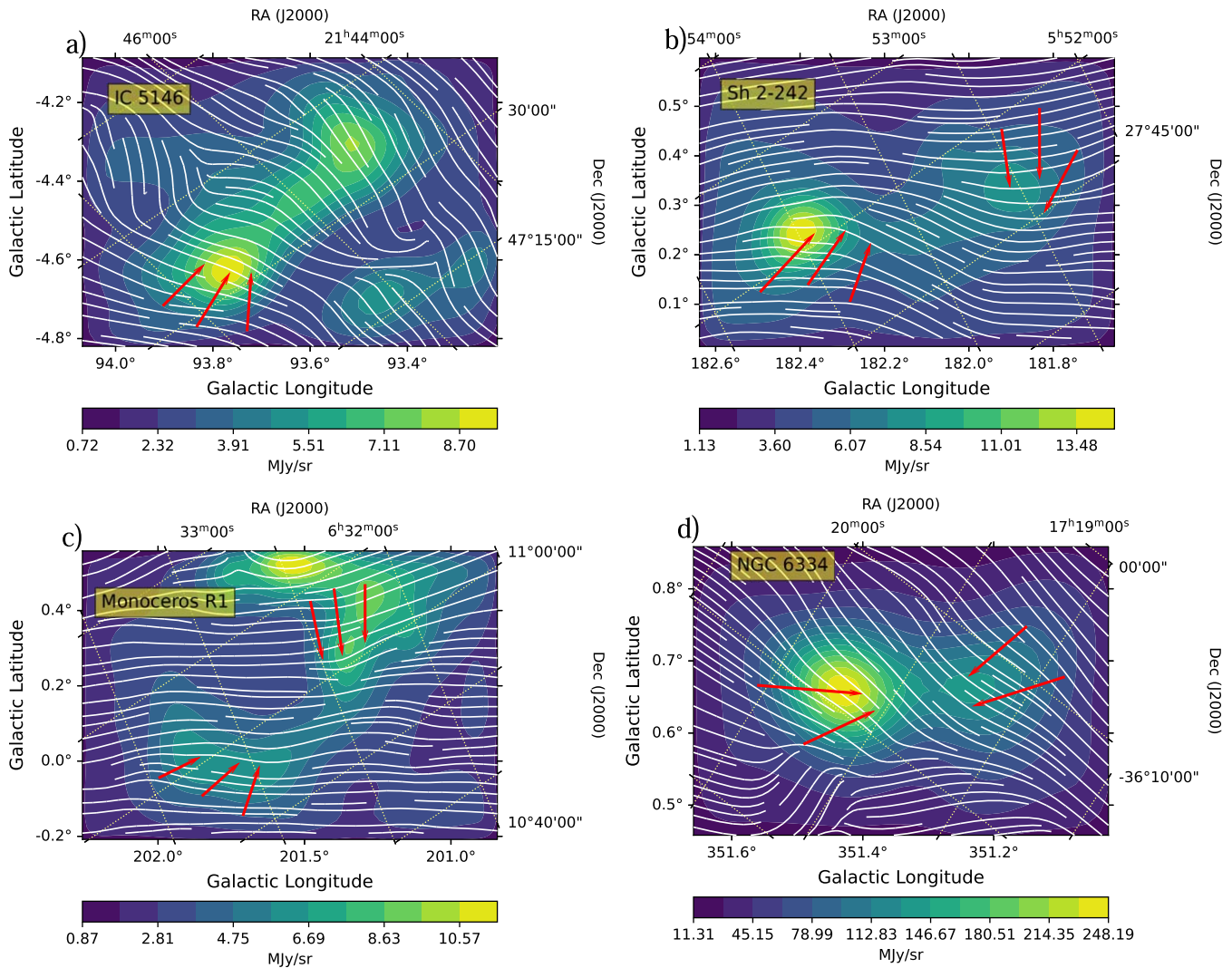


Figure 10. Planck 353 GHz Stokes- I images of EDC filaments IC 5146, Sh 2-242, Mon R1, and NGC 6334 overlaid by streamlines displaying the POS magnetic field. The streamlines are displayed using *streamplot* in *matplotlib* for a density parameter of 1.0. The red arrows indicate the B -field curvature at the filament edges. The Stokes Q and U maps were used to calculate the POS magnetic field position angles (see the text for more details).

and Chung et al. (2022), the B -field directions in the EDC filaments make a shapes of “)” and “(” at the filament edges (hereafter, the bending effect). This is because the material piles up at the edges, which itself moves toward the center of the filament (e.g., Clarke & Whitworth 2015). This longitudinal motion of gaseous material from the ends to the center of the filament can have sufficient ram pressure that pinches the magnetic field lines and forms the U-shaped magnetic field morphology (or bending effect; see more details in Gómez et al. 2018; Wang et al. 2019, 2020a). This effect is most prominently seen in the S242 and Mon R1 filament than in the other sources (e.g., IC 5146 dark streamer and NGC 6334; see the arrows in Figure 10). We suspect that the bending effect at one of the edges of the IC 5146 dark streamer is not prominent because of the contamination caused by the presence of the HFS. However, still, this effect is significant toward the southeastern clump of the IC 5146 dark streamer (see also Figure 7 of Chung et al. 2022). Similarly, NGC 6334 also shows the signature of an HFS at its edges (see Figure 2 of Tigé et al. 2017a) and does not show the strong bending effect shown in Figure 10. However, the high-resolution polarization map (beam $\sim 14''$) of NGC 6334 by

Arzoumanian et al. (2021) indeed shows the bending effect at the dense eastern region (Figure 10) revealing the longitudinal gas motion along the filament. The direction of the magnetic field at the other end of NGC 6334 is randomly oriented in the high-resolution map of Arzoumanian et al. (2021). However, our Planck magnetic field map shows the signature of curvature at this end, too (see Figure 10). It is discussed in the literature that the magnetic field distortions can be caused by the outflow-driven shocks, feedback from expanding ionized fronts, and gravity-driven gas flows (e.g., Arzoumanian et al. 2021; Eswaraiah et al. 2021). Also, recent observations signify that the curved magnetic field could have originated from the effect of gravity and the collision of clouds (e.g., Wang et al. 2020a, 2022). Therefore, it is quite possible that the intense star formation activity and the presence of HFSs at the filament edges can distort the initial bending effect in EDC filaments. Although our target filaments are promising EDC candidates, their nonlinearity can diminish the bending effect at low-resolution Planck magnetic field maps. Thus, we confirm that the other linear EDC filaments (if HFSs are not present) should show the bending effect.

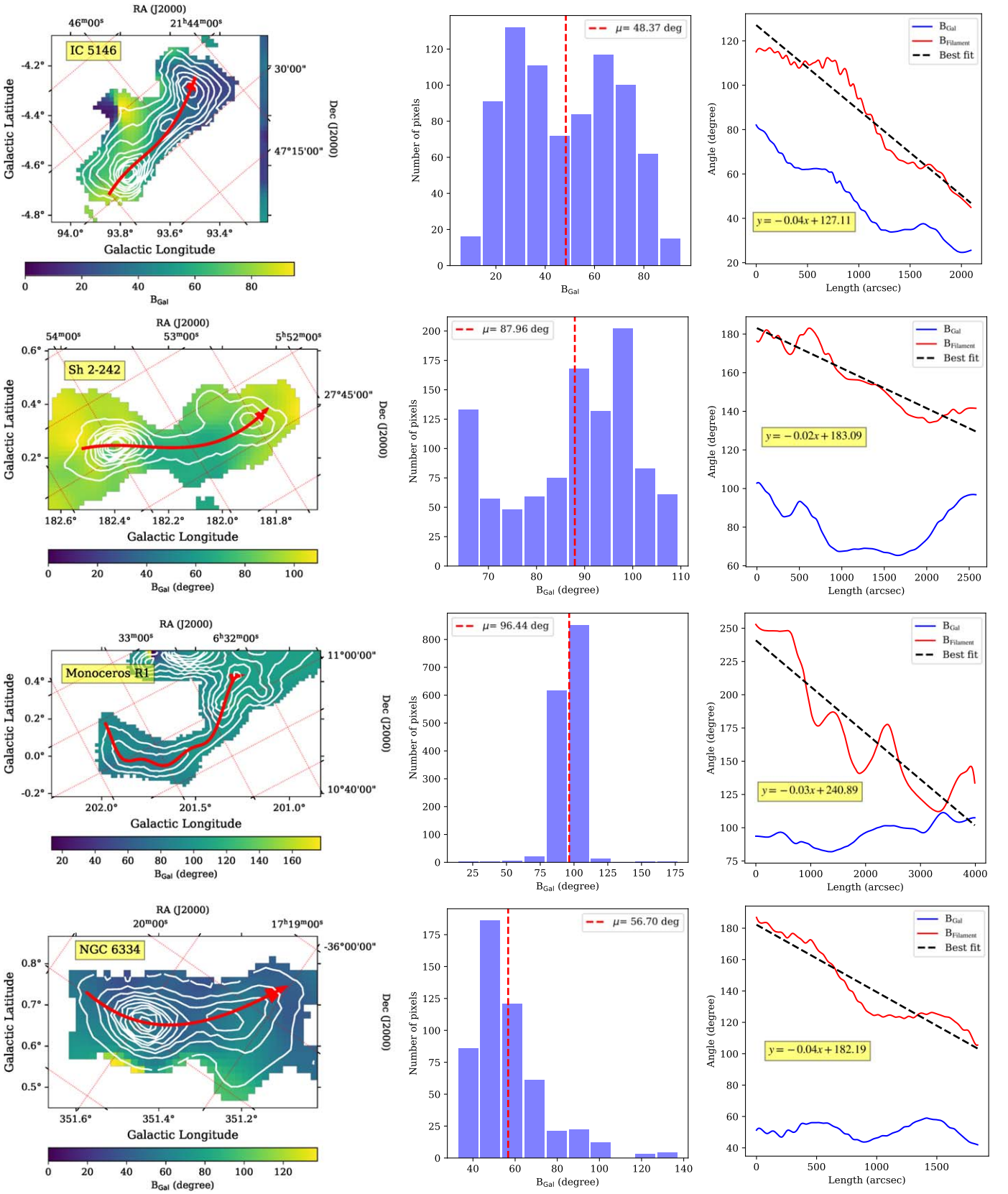


Figure 11. Distribution of the POS magnetic field angle with respect to the Galactic north to the counterclockwise direction (B_{Gal}) toward selected EDC filaments. The first column displays the spatial distribution of B_{Gal} of EDC filaments IC 5146, Sh 2-242, Mon R1, and NGC 6334. The overlaid contours refer to the Planck 353 GHz intensity (see Figure 10). The second column presents histograms of B_{Gal} corresponding to the targets shown in the first column. A vertical red-dashed line indicates the mean B_{Gal} of the histogram distribution. The third column displays the variation in B_{Gal} and B_{filament} along the long axis of filaments (see red curves in the first column). B_{filament} is the magnetic field position angle measured from the filament's major axis to the counterclockwise direction (see the text for more details). A best-fitted line for the B_{filament} distribution is shown and labeled.

Figure 11 displays the spatial distribution of the magnetic field position angle (B_{Gal}) toward selected EDC filaments. The derived B_{Gal} maps are masked out for regions of low intensity and used to obtain the histograms of B_{Gal} (see Column 2 of Figure 11). The mean B_{Gal} is found to be 48.37° , 87.96° , 96.44° , and 56.70° for the IC 5146 dark streamer, S242, Mon R1, and NGC 6334, respectively. To derive the B_{Gal} distribution in the IC 5146 dark streamer, we have considered only the region containing elongated filament. Hence, we have masked out the southwest region seen in Figure 10. Interestingly, these two filaments are nearly perpendicular to the Galactic plane. Mon R1, however, is a highly curved filament having its ends nearly perpendicular and parallel to the Galactic plane. A positive gradient in B_{Gal} can be seen from where the Mon R1 filament becomes perpendicular to the Galactic plane. The distribution of B_{Gal} along the long axis of selected filaments is denoted by blue curves in Figure 11. To quantify the distribution of the magnetic field toward the target filaments, we estimated the magnetic field position angle with respect to the filament's major axis from the direction of its head (B_{filament}). The distribution of B_{filament} versus filament's length ($B_{\text{filament}}-L$) is shown by red curves in Figure 11. Interestingly, for all the filaments, the global trend follows a negative slope in a range of $[-0.04, -0.02]$ deg arcsec $^{-1}$. We estimated the slope by fitting a straight line (see the black-dotted line) on the $B_{\text{filament}}-L$ plot. The negative slope in $B_{\text{filament}}-L$ distribution agrees well with the idea of the magnetic field bending effect by Wang et al. (2019). Ideally, a straight filament having magnetic field lines perpendicular toward its central regions and curved magnetic fields (i.e., shapes of “)” and “(”) toward the respective edges (see Figure 13 of Wang et al. 2019), should show the global increasing or decreasing trend in the $B_{\text{filament}}-L$ plot. The negative or positive trend will depend upon the choice of reference direction (i.e., filament's head or tail) from which the magnetic field angle is measured. In our target filaments, a global linear trend in the $B_{\text{filament}}-L$ plot hints at the EDC signature. However, despite the linear trend, we witness local oscillations as well. This is possible because of the nonlinearity of the filament (or sky-projection effect) and the contamination caused by other ongoing processes.

4.2. Physical Processes Operating in the IC 5146 Dark Streamer

Based on the examination of the TRAO molecular line data, a collision of turbulent converging flows has been suggested to explain the existence of HFSs, which also includes the role of mass flow along the filaments to the dense cores in IC 5146 (Chung et al. 2021). In order to further explore the collision process in the streamer, we revisited the TRAO ^{13}CO and C^{18}O line data (see Section 3.3). Our analysis of the molecular line data shows the existence of two cloud components around 2 and 4 km s $^{-1}$ in the direction of the IC 5146 dark streamer, and a velocity connection of these components is also found. The areas of the E-HFS and W-HFS, where the higher level of clumpiness is observed, are seen toward the common zones of the cloud components (see Section 3.3.2). Earlier works on the cloud-cloud collision (CCC) recommend a spatial and velocity connection of two cloud components as a reliable tracer of CCC (see Fukui et al. 2021; Maity et al. 2022, and references therein for more details). In general, colliding gas flows are thought to be operated in the low-density medium, while the

high-density phase of colliding gas flows could refer to CCC (e.g., Beuther et al. 2020; Dewangan 2022).

Central hubs of HFSs, hosting massive stars and clusters of YSOs, are thought to gain inflow material from very large scales of 1–10 pc, which can be funneled along molecular filaments (see Tigé et al. 2017b; Motte et al. 2018, for more details). Theoretical works favor the existence of HFSs by the colliding clouds or large-scale colliding flows (Balfour et al. 2015; Inoue et al. 2018), and this scenario is also supported in a recent review article on CCC (Fukui et al. 2021). Based on our findings, it is likely that the IC 5146 dark streamer may be influenced by the collision process, and both HFSs appear to be originated in the shock-compressed interface layer by the colliding clouds/flows (see also Chung et al. 2021). The massive sources are exclusively found to reside at the hub locations (see Figure 4).

We have examined why HFSs are formed at the edges of the filament fl . It has already been explained by the onset of the edge-driven collapse in the filament fl , which has a higher aspect ratio (see Wang et al. 2019; Chung et al. 2022, and references therein). In the EDC process, density enhancement is expected at each end of the filament due to high gas acceleration (Bastien 1983; Pon et al. 2012; Clarke & Whitworth 2015; Hoemann et al. 2022).

The present work reveals the existence of two coupled (or intertwined) sub-filaments (i.e., $fl-A$ and $fl-B$) toward the main filament fl , showing almost a double helix-like pattern (see Figures 3(d) and 4, and Section 3.1). The TRAO ^{13}CO and C^{18}O line data do not reveal this configuration due to a coarse beam size. However, the JCMT C^{18}O (3–2) map seems to support the detected structures in the Herschel maps. Hence, such intertwined configuration is seen in both dust and molecular emissions. A cartoon diagram displaying the physical configuration of sub-filaments $fl-A$ and $fl-B$ (Figure 3(d)) is motivated by their simultaneous detection in the dust continuum and the molecular emission maps. However, the existing molecular line data do not allow us to trace the velocity information along each sub-filament. Dewangan et al. (2021) found velocity oscillation along two intertwined filaments in the site LBN 140.07+01.64. The physical configuration of sub-filaments in the IC 5146 streamer appears very similar to the sub-filaments identified in LBN 140.07+01.64 (see Figures 3 and 7 in Dewangan et al. 2021). Therefore, due to the limited number of sites in the literature, the presence of intertwined filaments or their double helix-like pattern and their role in star formation demand more observational as well as theoretical insights. The sub-filaments $fl-A$ and $fl-B$ appear to spatially overlap each other along the major axis, forming multiple common areas where the Herschel clumps and YSOs are seen. This is another new outcome of this work. In this relation, we examined the existing *fray and fragment* scenario of the formation of intertwined substructures (Tafalla & Hacar 2015; Clarke et al. 2017), which first predicts the formation of the main filament by a collision of two supersonic turbulent gas flows, and then the scenario favors the origin of the intertwined system of velocity-coherent substructures in the main filament due to residual turbulent motions and self-gravity (see also Smith et al. 2014; Shimajiri et al. 2019). This scenario has been proposed in the NGC 6334 filament (Shimajiri et al. 2019) and the Taurus filament (Tafalla & Hacar 2015).

Additionally, we have also investigated a noticeable velocity oscillation along the filament fl (see Section 3.3.2). Previously, in the case of a filament G350.5-N associated with the cloud G350.54+0.69, Liu et al. (2019) reported a large-scale periodic velocity oscillation. To explain this aspect, on the basis of gravitational-instability-induced core formation models, they proposed a proposal with the combination of longitudinal gravitational instability and a large-scale physical oscillation along the filament. Considering two sub-filaments and the distribution of the Herschel clumps toward the long filament fl , the observed velocity oscillations/variations seem to support the presence of two coupled or intertwined sub-filaments and fragment/clump formation along the filament, where the nonthermal (or turbulent) pressure seems to be dominated (see Section 3.3.2).

Taken together, our findings reveal the onset of multiple physical processes in the IC 5146 dark streamer, which includes the edge collapse, CCC, accretion flows, and fray and fragment scenario.

5. Summary and Conclusions





In order to probe ongoing physical processes in a nearby star-forming site IC 5146 dark streamer ($d \sim 600$ pc), we conducted a study using the multiwavelength data. The dark streamer resembles a single and long filament, fl , having an aspect ratio >5 . The eastern and the western ends of fl harbor one HFS. Simultaneous detections of the HFSs and the edge collapse have been reported in the filament fl . High-resolution Herschel column density map (resolution $\sim 13''5$) is produced in this work and shows higher column densities toward both the HFSs. The Herschel column density map also displays two intertwined sub-filaments (i.e., $fl-A$ and $fl-B$) toward the main filament fl . Such configuration displays almost a double helix-like pattern, which is also seen in the integrated intensity map of the JCMT $C^{18}O(3-2)$ emission.

Using the TRAO $^{13}CO(1-0)$ and $C^{18}O(1-0)$ line data cubes, we have found the existence of two cloud components (around 2 and 4 km s^{-1}) toward the main filament. The cloud component around 4 km s^{-1} has an elongated appearance like the main filament fl . Both HFSs are spatially seen at the common regions of the cloud components. The origin of HFSs in fl may be explained by the CCC process. A careful analysis of the ^{13}CO and $C^{18}O$ emission shows the presence of nonthermal motion in fl with a larger Mach number. The central hub of the E-HFS shows higher values of $N(H_2)$, Mach number, and lower values of R_p compared to the W-HFS. The study of velocity profiles along the filament fl shows an oscillatory-like velocity pattern, favoring the presence of intertwined structures and fragments along fl . The origin of the intertwined substructures in fl seems to be explained by the fray and fragment scenario. The study of the Planck polarimetric maps of potential and nearby EDC filaments ($d \lesssim 2$ kpc) supports the detection of a curved magnetic field morphology as a signature for the edge collapse as discussed in Wang et al. (2019). In the IC 5146 dark streamer, we suspect that the bending effect of the magnetic field toward the western hub may be diminished by the presence of evolved HFS (i.e., W-HFS). The magnetic field position angle measured from the filament's major axis shows a linear trend along the filament. This signature is confirmed in the other nearby EDC filaments. Thus, this analysis may present a more quantitative observational proxy of the EDC scenario. Taking into account all our derived results, the IC

5146 dark streamer can be considered the first reliable candidate of edge collapse, HFSs, and intertwined sub-filaments.

We thank the anonymous reviewer for the constructive comments that improved the scientific content of the manuscript. The research work at Physical Research Laboratory is funded by the Department of Space, Government of India. C.W.L. is supported by the Basic Science Research Program through the National Research Foundation of Korea (NRF) funded by the Ministry of Education, Science and Technology (NRF-2019R1A2C1010851), and by the Korea Astronomy and Space Science Institute grant funded by the Korea government (MSIT; Project No. 2022-1-840-05). D. R. has been supported by the European Research Council advanced grant H2020-ER-2016-ADG-743029 under the European Unions Horizon 2020 Research and Innovation program. NKB thanks Jia-Wei Wang for providing useful comments on the manuscript. This research has made use of data from the Herschel Gould Belt survey (HGBS) project (<http://gouldbelt-herschel.cea.fr>). The HGBS is a Herschel Key Program jointly carried out by SPIRE Specialist Astronomy Group 3 (SAG 3), scientists of several institutes in the PACS Consortium (CEA Saclay, INAF-IFSI Rome, and INAF-Arcetri, KU Leuven, MPIA Heidelberg), and scientists of the Herschel Science Center (HSC). This research made use of *Astropy*,⁹ a community-developed core Python package for Astronomy (Astropy Collaboration et al. 2013, 2018, 2022) and *matplotlib* (Hunter 2007) Python package.

ORCID iDs

L. K. Dewangan  <https://orcid.org/0000-0001-6725-0483>
 N. K. Bhadari  <https://orcid.org/0000-0001-8812-8460>
 A. Men'shchikov  <https://orcid.org/0000-0001-5201-5595>
 E. J. Chung  <https://orcid.org/0000-0003-0014-1527>
 R. Devaraj  <https://orcid.org/0000-0001-9217-3168>
 C. W. Lee  <https://orcid.org/0000-0002-3179-6334>
 A. K. Maity  <https://orcid.org/0000-0002-7367-9355>
 T. Baug  <https://orcid.org/0000-0003-0295-6586>

References

- André, P., Men'shchikov, A., Bontemps, S., et al. 2010, *A&A*, **518**, L102
 Arzoumanian, D., André, P., Didelon, P., et al. 2011, *A&A*, **529**, L6
 Arzoumanian, D., André, P., Könyves, V., et al. 2019, *A&A*, **621**, A42
 Arzoumanian, D., André, P., Peretto, N., & Könyves, V. 2013, *A&A*, **553**, A119
 Arzoumanian, D., Furuya, R. S., Hasegawa, T., et al. 2021, *A&A*, **647**, A78
 Assirati, L., Silva, N. R., Berton, L., Lopes, A. A., & Bruno, O. M. 2014, *JPhCS*, **490**, 012020
 Astropy Collaboration, Price-Whelan, A. M., Lim, P. L., et al. 2022, *ApJ*, **935**, 167
 Astropy Collaboration, Price-Whelan, A. M., Sipőcz, B. M., et al. 2018, *AJ*, **156**, 123
 Astropy Collaboration, Robitaille, T. P., Tollerud, E. J., et al. 2013, *A&A*, **558**, A33
 Balfour, S. K., Whitworth, A. P., Hubber, D. A., & Jaffa, S. E. 2015, *MNRAS*, **453**, 2471
 Bastien, P. 1983, *A&A*, **119**, 109
 Bell, G. S. 2008, PhD Thesis, Univ. College London
 Beuther, H., Wang, Y., Soler, J., et al. 2020, *A&A*, **638**, A44
 Bhadari, N. K., Dewangan, L. K., Ojha, D. K., Pirogov, L. E., & Maity, A. K. 2022, *ApJ*, **930**, 169
 Bhadari, N. K., Dewangan, L. K., Pirogov, L. E., & Ojha, D. K. 2020, *ApJ*, **899**, 167

⁹ <http://www.astropy.org>

- Buckle, J. V., Hills, R. E., Smith, H., et al. 2009, *MNRAS*, **399**, 1026
- Chung, E. J., Lee, C. W., Kim, S., et al. 2021, *ApJ*, **919**, 3
- Chung, E. J., Lee, C. W., Kwon, W., et al. 2022, *ApJ*, **164**, 175
- Clarke, S. D., & Whitworth, A. P. 2015, *MNRAS*, **449**, 1819
- Clarke, S. D., Whitworth, A. P., Duarte-Cabral, A., & Hubber, D. A. 2017, *MNRAS*, **468**, 2489
- Condon, J. J., Cotton, W. D., Greisen, E. W., et al. 1998, *AJ*, **115**, 1693
- Cox, N. L. J., Arzoumanian, D., André, P., et al. 2016, *A&A*, **590**, A110
- Dewangan, L. K. 2022, *MNRAS*, **513**, 2942
- Dewangan, L. K., Dhanya, J. S., Bhadani, N. K., Ojha, D. K., & Baug, T. 2021, *MNRAS*, **506**, 6081
- Dewangan, L. K., Ojha, D. K., Zinchenko, I., Janardhan, P., & Luna, A. 2017, *ApJ*, **834**, 22
- Dewangan, L. K., Pirogov, L. E., Ryabukhina, O. L., Ojha, D. K., & Zinchenko, I. 2019, *ApJ*, **877**, 1
- Dobashi, K., Onishi, T., Iwata, T., et al. 1993, *AJ*, **105**, 1487
- Eswaraiah, C., Li, D., Furuya, R. S., et al. 2021, *ApJL*, **912**, L27
- Fukui, Y., Habe, A., Inoue, T., Enokiya, R., & Tachihara, K. 2021, *PASJ*, **73**, S1
- Gómez, G. C., Vázquez-Semadeni, E., & Zamora-Avilés, M. 2018, *MNRAS*, **480**, 2939
- Hacar, A., Tafalla, M., Forbrich, J., et al. 2018, *A&A*, **610**, A77
- Hacar, A., Tafalla, M., Kauffmann, J., & Kovács, A. 2013, *A&A*, **554**, A55
- Harvey, P. M., Huard, T. L., Jørgensen, J. K., et al. 2008, *ApJ*, **680**, 495
- Herbig, G. H., & Reipurth, B. 2008, in *Handbook of Star Forming Regions*, Volume I. The Northern Sky, ed. B. Reipurth, Vol. 4 (San Francisco, CA: ASP), 108
- Hoemann, E., Heigl, S., & Burkert, A. 2022, arXiv:2203.07002
- Hunter, J. D. 2007, *CSE*, **9**, 90
- Inoue, T., Hennebelle, P., Fukui, Y., et al. 2018, *PASJ*, **70**, S53
- Inutsuka, S.-i., Inoue, T., Iwasaki, K., & Hosokawa, T. 2015, *A&A*, **580**, A49
- Johnstone, D., Ciccone, S., Kirk, H., et al. 2017, *ApJ*, **836**, 132
- Kramer, C., Richer, J., Mookerjee, B., Alves, J., & Lada, C. 2003, *A&A*, **399**, 1073
- Lada, C. J., Bergin, E. A., Alves, J. F., & Huard, T. L. 2003, *ApJ*, **586**, 286
- Lada, C. J., Lada, E. A., Clemens, D. P., & Bally, J. 1994, *ApJ*, **429**, 694
- Liu, H.-L., Stutz, A., & Yuan, J.-H. 2019, *MNRAS*, **487**, 1259
- Maity, A. K., Dewangan, L. K., Sano, H., et al. 2022, *ApJ*, **934**, 2
- Men'shchikov, A. 2021, *A&A*, **649**, A89
- Motte, F., Bontemps, S., & Louvet, F. 2018, *ARA&A*, **56**, 41
- Myers, P. C. 2009, *ApJ*, **700**, 1609
- Nakamura, F., & Li, Z.-Y. 2008, *ApJ*, **687**, 354
- Onishi, T., Mizuno, A., Kawamura, A., Tachihara, K., & Fukui, Y. 2002, *ApJ*, **575**, 950
- Palmeirim, P., André, P., Kirk, J., et al. 2013, *A&A*, **550**, A38
- Planck Collaboration, Ade, P. A. R., Aghanim, N., et al. 2014, *A&A*, **571**, A9
- Planck Collaboration, Ade, P. A. R., Aghanim, N., et al. 2015, *A&A*, **576**, A104
- Planck Collaboration, Ade, P. A. R., Aghanim, N., et al. 2016a, *A&A*, **586**, A138
- Planck Collaboration, Ade, P. A. R., Aghanim, N., et al. 2016b, *A&A*, **586**, A136
- Planck Collaboration, Ade, P. A. R., Aghanim, N., et al. 2016c, *A&A*, **594**, A19
- Planck Collaboration, Adam, R., Ade, P. A. R., et al. 2016d, *A&A*, **594**, A8
- Pon, A., Toalá, J. A., Johnstone, D., et al. 2012, *ApJ*, **756**, 145
- Roy, A., Ade, P. A. R., Bock, J. J., et al. 2011, *ApJ*, **730**, 142
- Saito, H., Saito, M., Moriguchi, Y., & Fukui, Y. 2006, *PASJ*, **58**, 343
- Shimajiri, Y., André, P., Ntormousi, E., et al. 2019, *A&A*, **632**, A83
- Smith, R. J., Glover, S. C. O., & Klessen, R. 2014, *MNRAS*, **445**, 2900
- Tafalla, M., & Hacar, A. 2015, *A&A*, **574**, A104
- Tigé, J., Motte, F., Russeil, D., et al. 2017a, *A&A*, **602**, A77
- Tigé, J., Motte, F., Russeil, D., et al. 2017b, *A&A*, **602**, A77
- Wang, J.-W., Koch, P. M., Galván-Madrid, R., et al. 2020a, *ApJ*, **905**, 158
- Wang, J.-W., Koch, P. M., Tang, Y.-W., et al. 2022, *ApJ*, **931**, 115
- Wang, J.-W., Lai, S.-P., Clemens, D. P., et al. 2020b, *ApJ*, **888**, 13
- Wang, J.-W., Lai, S.-P., Eswaraiah, C., et al. 2017, *ApJ*, **849**, 157
- Wang, J.-W., Lai, S.-P., Eswaraiah, C., et al. 2019, *ApJ*, **876**, 42
- Williams, J. P., de Geus, E. J., & Blitz, L. 1994, *ApJ*, **428**, 693
- Yu, N.-P., Xu, J.-L., & Wang, J.-J. 2019, *A&A*, **622**, A155
- Yuan, L., Li, G.-X., Zhu, M., et al. 2020, *A&A*, **637**, A67
- Zernickel, A., Schilke, P., & Smith, R. J. 2013, *A&A*, **554**, L2
- Zhang, S., Yang, J., Xu, Y., et al. 2020, *ApJS*, **248**, 15